Supplementary Information for

Superior Electrochemical Performance of Alkali Metal Anodes Enabled by Milder Lewis Acidity

Linlin Wang‡ [a], Jiacheng Zhu‡ [b], Nan Li [a], Zhe Zhang [a], Shiwan Zhang, [a] Yifan Chen [a], Jianwen Zhang [a], Yusi Yang [a], Lulu Tan [a], Xiaogang Niu [a], Xuefeng Wang [b], Xiao Ji* [c], and Yujie Zhu* [a, d]*

[a] School of Chemistry, Beihang University, Beijing 100191, People's Republic of China

[b] Institute of Physics, Chinese Academy of Sciences, College of Materials Science and Opto-Electronic Technology, University of Chinese Academy of Sciences, Beijing 100190, People's Republic of China

[c] School of Optical and Electronic Information, Huazhong University of Science and Technology, Wuhan, Hubei 430074, People's Republic of China

[d] Beijing Advanced Innovation Center for Biomedical Engineering, Beihang University, Beijing 100191, People's Republic of China

Materials and Electrolytes

Lithium metal sheet (15.6 x 0.45 mm), sodium metal sheet (14 x 0.45 mm), lithium bis(fluorosulfonyl)imide (LiFSI, purity ≥99.9%), sodium bis(fluorosulfonyl)imide (NaFSI, purity ≥ 99.9%), and triethyl phosphate (TEP, purity ≥ 99.9%) were procured from Suzhou Duoduo Chemical Technology Co., Ltd. Potassium metal ingot, ferrocene (Fc, purity ≥99%), and 1,1,2,2-tetrafluoroethyl-2,2,3,3-tetrafluoropropyl ether (TTE, purity ≥ 99%) were obtained from Beijing InnoChem Science & Technology Co., Ltd. The Li, Na, and K electrolytes were prepared by dissolving corresponding 1M LiFSI, NaFSI, and KFSI, respectively, in a mixture of TEP and TTE (1:1 vol.%), designated as 1M LTT, 1M NTT, and 1M KTT. These preparations were

conducted in an argon-filled glovebox (with O_2 and H_2O content maintained below 0.01 ppm) at room temperature. Copper (Cu) foil (thickness ~12 μm) and aluminum (Al) foil (thickness ~9 μm) were sourced from Canrd Technology Co. Ltd. Before use, these foils were subjected to ultrasonic cleaning in ethanol for half an hour to remove oil residues from the production process, followed by drying at 80 °C for 12 h under vacuum conditions. The $K_2MnFe(CN)_6$ (KMF) material was synthesized following the procedure outlined in a previous publication by our research group.[1]

Electrochemical Measurements

All CR2032-type coin cells used for electrochemical testing were assembled within an argon-filled glove box with oxygen and water concentrations maintained below 0.01 ppm. Glass microfiber filters (diameter: 16 mm, Whatman, grade GF/D) were employed as separators for Li|Cu, Na|Al, and K|Al cells. For the plating-stripping tests in all alkali metal cells, a volume of 100 μL of the corresponding electrolyte was used. During these tests, once a specific capacity was plated onto the Al or Cu foil, the cells were charged to 1 V to complete the stripping process. The KMF cathode was prepared by coating a slurry containing KMF, acetylene black and polyvinylidene fluoride (PVDF) in a weight ratio of 70:20:10 onto Al foil, with a KMF loading of ~2 mg cm^{-2}. The KMF cathode were then punched into discs with an 11 mm diameter and used after vacuum drying at 80 °C for 10 h. For the cycling stability tests of the K|KMF cells (with an anode-to-cathode capacity (N/P) ratio of 2 and 60 μL electrolyte), they were initially subjected to charge-discharge cycling at 0.1 C (1 C = 150 mAh g^{-1}) for 20 cycles between 2.7 and 4.4 V (*vs.* K^+/K), and then the current density was adjusted to 0.5 C for the subsequent charge-discharge cycles using the NEWARE battery test system (CT-4008T-5V10mA-164, Shenzhen, China) and Land battery testing system (CT2001A, Wuhan LAND electronics, China). The K metal used in the K|KMF cells was obtained by electrochemically depositing 0.6 mAh cm^{-2} K metal onto the Al foil in the K|Al cells. All electrochemical cycling tests were carried out in an incubator (ZY6046-80CT, ZONSKY INSTRUMENTS Co., Ltd.) with controlled temperatures at 25 ± 0.5 °C. Electrochemical impedance spectroscopy (EIS) tests for alkali metal cells were

conducted using the Solartron Analytical electrochemical workstation (Solartron Mobrey, 1470E, England) with 5 mV sinusoidal amplitudes and a frequency range from 100,000 to 0.01 Hz. All EIS tests were performed after completely plating the alkali metal on the current collector (Al foil or Cu foil). In the assessment of electrode potentials for the alkali metals, three-electrode coin-type cells were employed. Within these cells, the alkali metal served as the reference electrode, platinum electrodes were designated as both working and counter electrodes, and 50 mM ferrocene was incorporated into all three electrolytes.

Characterizations

Electrolyte conductivity measurements were conducted at room temperature (25 °C) using a DDS-307A conductivity spectrometer. Each sample was subjected to three independent tests. Viscosity assessments of the electrolytes were performed employing the Anton Paar MCR-302 Viscometer, within a temperature ranging from -5 °C to 60 °C, with a heating rate of 3 °C min^{-1}. Raman spectra were obtained at room temperature with a Horiba LabRAM HR800 equipped with a 633 nm excitation laser (laser power of 5.1 mW) and a grating with 600 lines per mm. Following spectrum collection, baseline correction was applied, and peak intensities were normalized with respect to the highest intensity peak. Nuclear magnetic resonance (NMR) spectra for both pure solvent and electrolytes were recorded using a 500 MHz Bruker Avance III HD spectrometer. The deuterated reagent was prepared using anhydrous dimethyl sulfoxide (DMSO). To avert potential interactions between the deuterated reagent and the solvent, the solvent was loaded into a 3 mm NMR tube, which was subsequently placed within a 5 mm outer NMR tube, with the intervening space filled with DMSO. ^{13}C-NMR measurements were performed. All electrolytes used for conductivity, viscosity, Raman spectroscopy, and NMR were meticulously prepared within a glove box and allowed to equilibrate thermally for a period of 12 h.

Characterization of the plated alkali metal surface was conducted using a field emission scanning electron microscope (JEOL, JSM-7500F) operated at 5 kV. X-ray photoelectron spectroscopy (XPS) measurements were performed utilizing the Thermo

Scientific ESCALAB 250 Xi XPS system with Al Kα X-ray radiation (1361 eV) and a spot size of 400 μm (diameter) during acquisition. Survey scans were conducted with a 1.0 eV step, and high-resolution scans for the C 1s, F 1s, O 1s, and P 2p regions were performed with a 0.05 eV step size. All peaks were subjected to fitting after applying a correction based on the C-C bond at 284.8 eV. Deep etching was carried out using an Ar^+ source with an acceleration voltage of 2 kV and an incidence angle of 45°. The etching rate was determined to be 0.29 nm/s (*vs*. Ta_2O_5), with each etching lasting 25 seconds, and a total of two etchings were performed. The time-of-flight secondary-ion mass spectrometry (ToF-SIMS) measurements were conducted using a ToF-SIMS 5-100 instrument (IONTOF GmbH) to analyze the solid electrolyte interphase (SEI). The depth profiling was performed using a Bi^+ analysis ion beam (30 keV, 0.75 pA), raster size of 50 μm x 50 μm. The Cs^+ beam (1 keV, 60 nA) was used to sputter with a raster area of 200 μm x 200 μm, and a sputter rate of ~0.84 nm/s (*vs*. GaN), which reduces the work function of the material, thereby increasing the yield of negative secondary ion. Due to the different thicknesses of SEI, the sputtering time of Li and K metal is 1000 s, while the sputtering time of Na metal is 1500 s. The Surface Lab 7 software was used to plot the ToF-SIMS data into a 3D heat map. All test samples for SEM, XPS, and ToF-SIMS were prepared after subjecting the cells to 20 cycles of pre-cycling. The cells were disassembled in a glove box, washed with TEP solvent to eliminate residual salt on the surface, and subsequently dried in the glove box for 24 hours. To prevent exposure to air during sample transfer, all samples were hermetically sealed in test glass bottles. Cryogenic transmission electron microscopy (cryo-TEM) characterization was performed utilizing microscope (JEOL JEM F200) with cryogenic temperatures (-95.15K) at 200 kV. For the test samples of cryo-TEM, first, the three alkali metals were deposited onto a Cu-TEM grids at 0.1 mA cm^{-2} under an areal capacity of 0.2 mAh cm^{-2}. Subsequently, within a glovebox filled with argon, the TEM grids were transferred to a cryogenic vacuum transfer holder (Fischione 2555), which includes specially designed sealed shutters to ensure an entirely argon environment during the transfer process, preventing contact with air or liquid nitrogen. Then, the holder was inserted into the TEM chamber, and liquid nitrogen was added to the holder's Dewar flask for

cooling, achieving an internal temperature of approximately 91.15 K. Finally, the cryo-TEM images were analyzed using Digital Micrograph (Gatan) software.

Theoretical Calculations

All the classic molecular dynamic (cMD) simulations conducted in this work were performed using the Large-scale Atomic/Molecular Massively Parallel Simulator (LAMMPS, http://lammps.sandia.gov). All-atom optimized potentials for liquid simulations (OPLS-AA) force-field with the K^+ and FSI^- anions description from previous publications,[2, 3] while the force-field of TEP and TTE were obtained from the LigParGen[4] The electrolyte systems were setup initially with the salt and solvent molecules distributed in the simulation boxes using Packmol[5] and Moltemplate (http://www.moltemplate.org/)[6]. For each system, an initial energy minimization at 0 K (energy and force tolerances of 10^{-5}) was performed to obtain the ground-state structure. After this, the system was heated from 0 K to room temperature (300 K) at constant volume over 0.2 ns using a Langevin thermostat, with a damping parameter of 100 ps. The system was equilibrated in the constant temperature (300 K), constant pressure (1 bar) (NpT ensemble) for 5 ns. Finally, a MD run in the NVT ensemble was performed for 5 ns for equilibrium, and a following 5 ns NVT simulation was used for analysis.

Quantum chemistry calculations were performed using Gaussian 16 software package[7]. Geometry optimizations and energy calculations were performed using B3LYP/6-311G(d,p). The PCM continuum solvation model was used to implicitly represent solvent (ether). The binding energies (G_b) between the Li^+, Na^+, K^+ cations and TEP solvent are calculated as $G_b=G_{cation\text{-}TEP}-G_{cation}-G_{TEP}$, where $G_{cation\text{-}TEP}$, G_{cation}, and G_{TEP} are the free energies of the cation-TEP complex, cation, and TEP solvent, respectively. Here, a more negative binding energy indicates a more stable solvation structure. The visualization of the energy levels were made by using Multiwfn software[8].

Note S1. Calculation of dissociation coefficient of the salts in the three electrolytes.

The ion-pair dissociation coefficient α can be estimated using the following equation[9, 10]:

$$\alpha = \frac{\Lambda \eta}{\Lambda^{\infty} \eta^{\infty}} \quad (1)$$

where η and η^{∞} are the viscosity of the electrolytes and mixed solvents, respectively. Λ and Λ^{∞} are the molar conductivity and limiting molar conductivity which can be obtained from the Debye-Hückel-Onsager equation[11, 12]:

$$\Lambda^{\infty} = \Lambda - B\sqrt{C} \quad (2)$$

where B is the slope of the plot of Λ *vs.* $\sqrt{C}$ (with the electrolytes concentration C in the range of $10^{-3} \leqq C \leqq 10^{-2}$ mol L^{-1}). The plots of Λ *vs.* $\sqrt{C}$ for three electrolytes are presented in Fig. 1d, and they all display well-defined linear relationships. This indicates the applicability of Eq. (2) to the current electrolyte systems.

Note S2. Method for calculating cation transference number of electrolytes.

The method proposed by Gasteiger *et al*.,[13-15] was employed, which is designed for general electrolytes and involves two distinct steps:

i) A concentration coin cell was employed to measure the open circuit voltage between the alkali metal electrodes, exploiting the variance in salt concentrations. This approach leaded to the determination of the transport factor a .

$$a = \frac{F \cdot U_{CC}}{2RT} \cdot \frac{1}{\ln\left(\frac{c_0 + \Delta c}{c_0 - \Delta c}\right)} \tag{3}$$

where U_{CC} is the concentration cell potentials, F is the Faraday constant, R is universal gas constant, T is absolute temperature at the time of testing, c_0 is the concentration of the electrolytes being measured, and Δc is concentration difference.

ii) A symmetrical coin cell, featuring two alkali metal electrodes, was employed to monitor potential transients following a constant galvanostatic pulse, thereby allowing for the determination of the transport factor b .

$$b = \sqrt{\frac{d^2}{\pi^2} \cdot m_{\ln}} \cdot \frac{\sqrt{\pi} F^2}{8RT} \cdot A \cdot \varepsilon \cdot c_0 \frac{U(t_1)}{I_P \sqrt{t_1}} \tag{4}$$

where d is the thickness of separator, $m_{\ln}$ is the slope of the logarithm of the potential against time after a galvanostatic pulse, A is the area of the electrode, ε is the void volume fraction of the separator, c_0 is the concentration of the electrolyte being measured, $U(t_1)$ is the potential at the end of a galvanostatic pulse, t_1 is the duration of the applied galvanostatic pulse , I_P is the value of the pulse current.

Then, the cation transference number can be obtained by equation (5).

$$t_+ = 1 - \frac{b}{a} \tag{5}$$

The detailed experimental results pertaining to steps i) and ii) are presented in Fig. S1 and S2. The cell parameters utilized in Eqs. (3) and (4) can be found in Table S2.

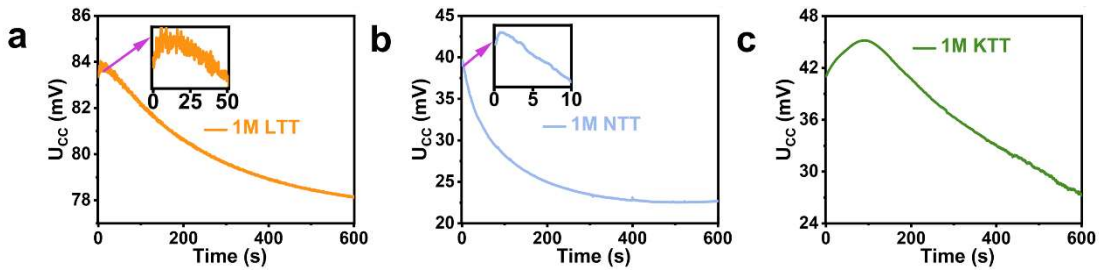

Fig. S1 (a-c) The potentials of concentration cells of corresponding electrolytes, (insets: the enlarged view of potentials) and the highest point of the voltage were taken as the concentration potentials for subsequent calculation.

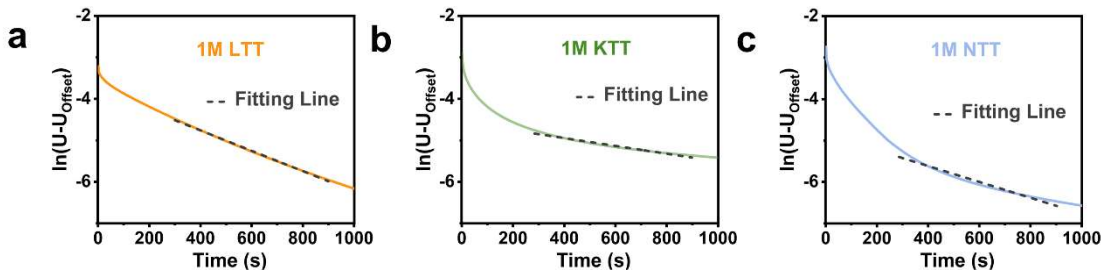

Fig. S2 (a-c) The logarithm of the potential against time after a galvanostatic pulse (0.3 mA for 15 min), and U_{offset} is the average of the records for the last five minutes of the relaxation period of 3.75 h. In order to ensure the consistency of comparison, the fitting interval of three electrolytes is 300 s-900 s.

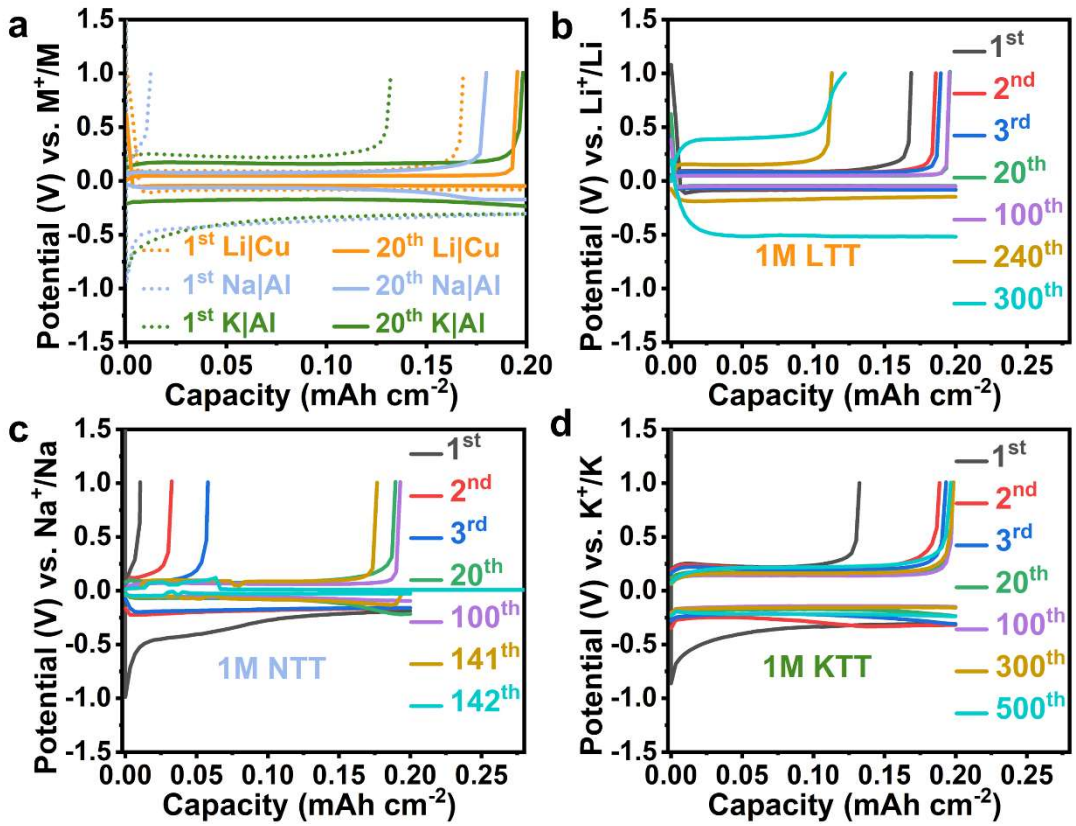

Fig. S3 (a-d) Plating-stripping curves of the Li|Cu, Na|Al and K|Al cells at 0.2 mA cm^{-2} under an areal capacity of 0.2 mAh cm^{-2}. Note: M = Li, Na and K.

During the initial plating process, the Li|Cu cell exhibits the lowest nucleation barrier (~ 114 mV) while the K|Al and Na|Al cells display comparable values (~ 862 mV for K and ~ 957 mV for Na) (Fig. S3a). This discrepancy may be attributed to the limited wettability of K and Na with respect to Al, as previously reported by Mitlin *et al.*[16] Subsequently, between the 20th and 100th cycles, the average CE is 97.97% for the Li|Cu cell, 96.38% for the Na|Al cell, and the highest for the K|Al cell (~99.15%) (as shown in Table S3). During extended cycling stability tests, the average CE for the Li|Cu cell over 240 cycles stood at 88.05% (Fig. S4). Fig. S4 illustrates a gradual decrease in CE for the Li|Cu cell after 160 cycles, accompanied by a progressive increase in plating-stripping overpotential (as depicted in Fig. S3b). For the Na|Al cell, the average CE reached 93.34% over 139 cycles, but it experienced a short-circuit failure at the 140th cycle (as seen in Fig. S3c).

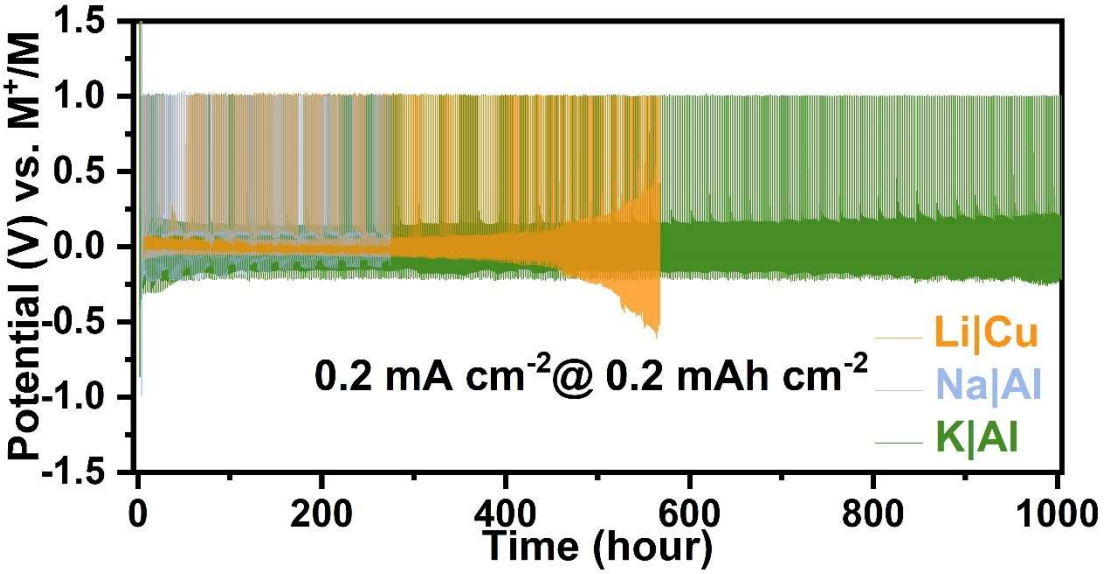

Fig. S4 The voltage-time curves of the Li|Cu, Na|Al and K|Al cells at 0.2 mA cm^{-2} under an areal capacity of 0.2 mAh cm^{-2}. Note: M = Li, Na and K.

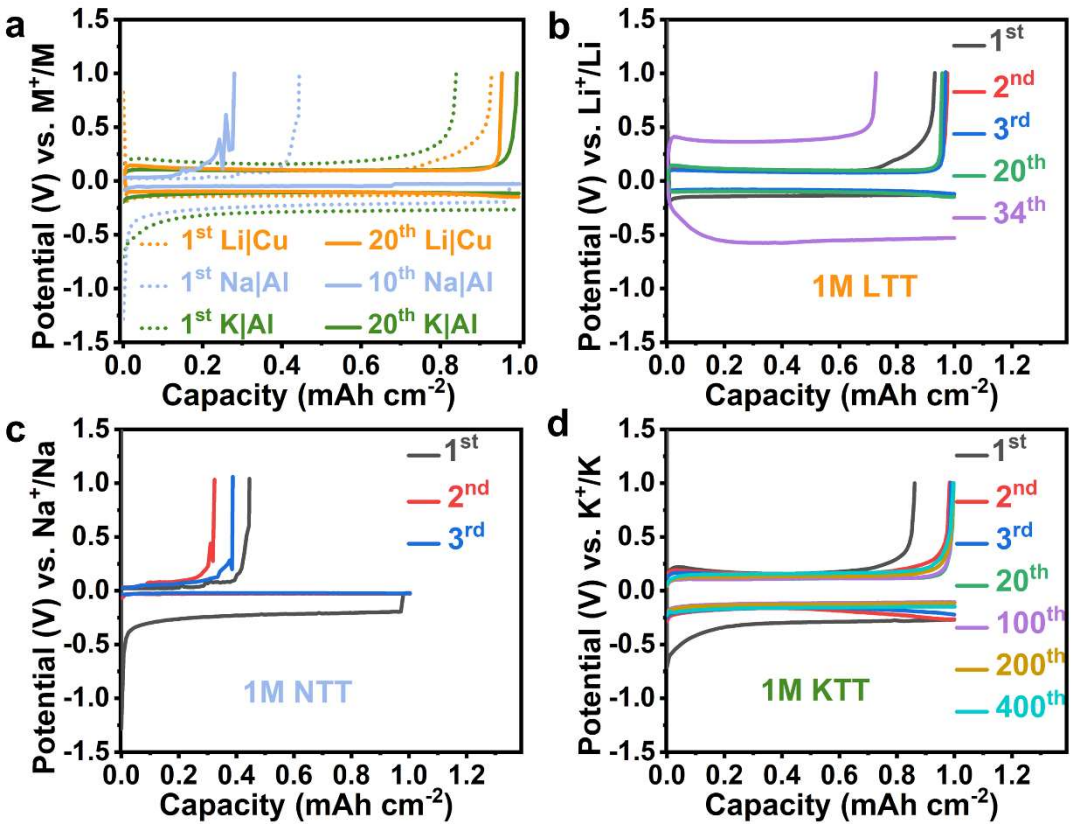

Fig. S5 (a-d) Plating-stripping curves of the Li|Cu, Na|Al and K|Al cells at 0.5 mA cm^{-2} under an areal capacity of 1 mAh cm^{-2}. Note: M = Li, Na and K.

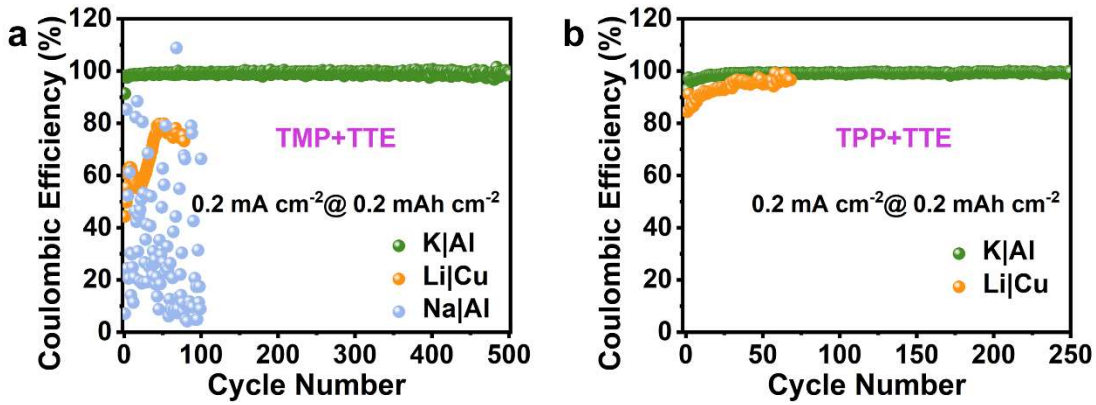

Fig. S6 (a) Coulombic efficiency of the Li|Cu, Na|Al and K|Al cells at 0.2 mA cm^{-2} under an areal capacity of 0.2 mAh cm^{-2} using trimethyl phosphate (TMP) and TTE as solvents. (b) Coulombic efficiency of the Li|Cu, Na|Al and K|Al cells at 0.2 mA cm^{-2} under an areal capacity of 0.2 mAh cm^{-2} using tripropyl phosphate (TPP) and TTE as solvents. In this case, Na metal could not be reliably plated.

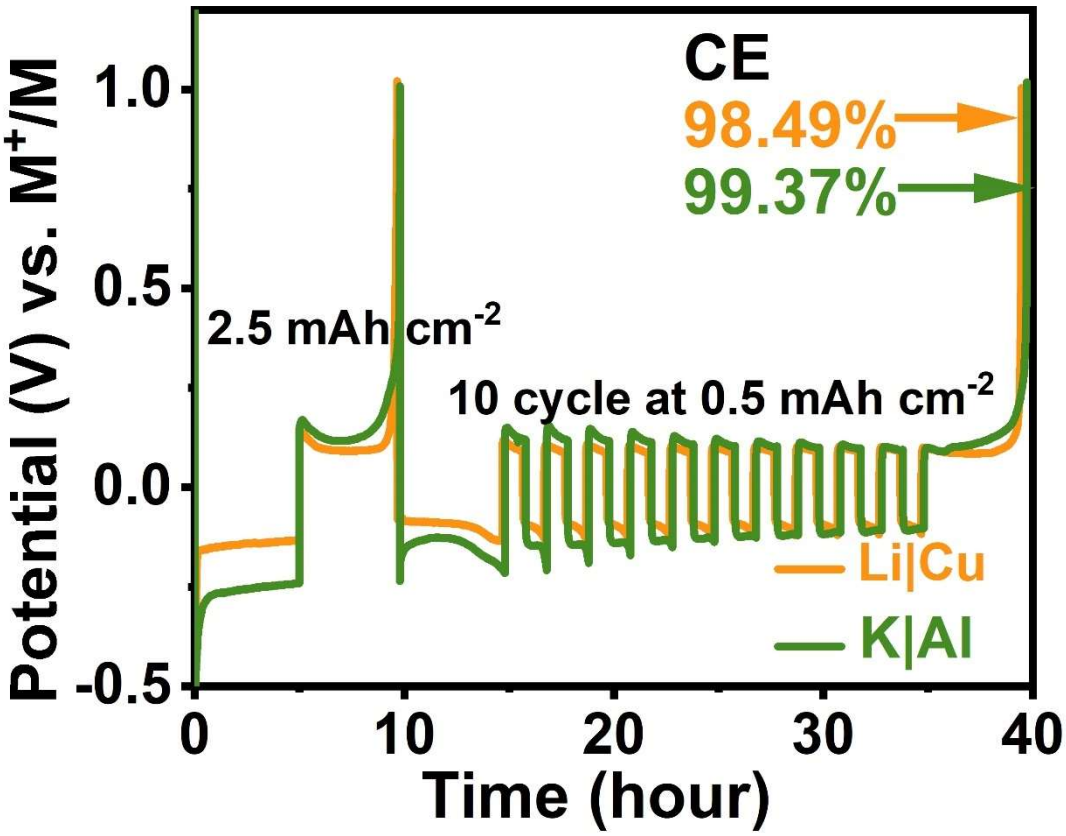

Fig. S7 The average CE for the K|Al and Li|Cu cells tested by the Zhang *et al.*'s approach. This test of the average CE was conducted as follows: first, the alkali metal was plated and stripped at a high plating capacity of 2.5 mAh cm^{-2} and a low current density of 0.5 mA cm^{-2} for 1 cycle; second, the alkali metal was electroplated onto the current collector at a plating capacity of 2.5 mAh cm^{-2}, then repeatedly stripped-plated under a low capacity of 0.5 mAh cm^{-2} and a current density of 0.5 mA cm^{-2} for 10 cycles, and finally stripped to the designated cutoff potential (1 V). Note: M = Li, and K. The average Coulombic efficiency was calculated according to the following equation:

$$CE_{avg} = \frac{nQ_C + Q_S}{nQ_C + Q_T} \tag{6}$$

Where n is the cycle number of repeatedly stripped-plated Li or K, Q_C is the capacity of repeatedly stripped-plated Li or K, Q_T is the capacity of the pre-plated Li or K, and Q_S is the capacity of finally stripped Li or K.

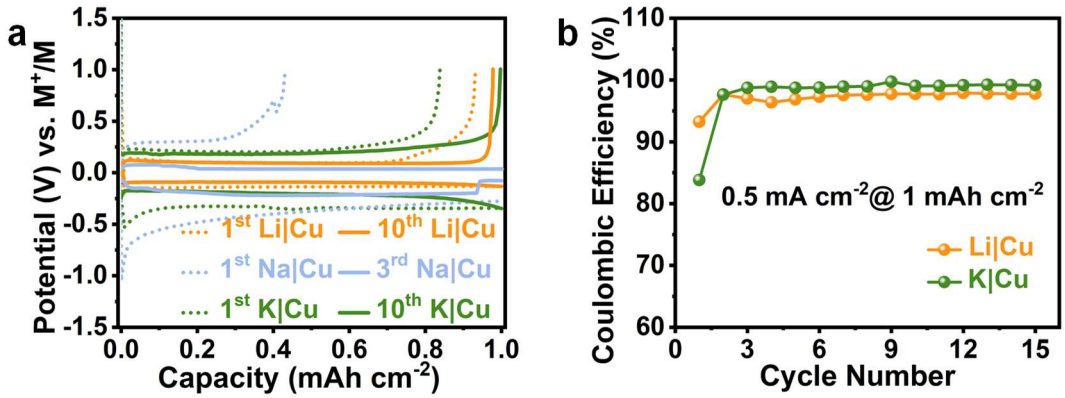

Fig. S8 (a) Plating-stripping curves of the Li|Cu, Na|Cu and K|Cu cells at 0.5 mA cm^{-2} under an areal capacity of 1 mAh cm^{-2}; (b) Coulombic efficiency of the Li|Cu and K|Cu cells at 0.5 mA cm^{-2} under an areal capacity of 1 mAh cm^{-2} using Cu foil as current collector. Note: M = Li, Na and K in (a).

As shown in Fig. S8, when Cu is used as the current collector for Li, Na, and K cells, it can be observed that Na also cannot be reliably plated onto Cu foil, leading to a short circuit in the third cycle (Fig. S8a). The Coulombic efficiency of K|Cu remains superior to that of Li|Cu (Fig. S8b). Under the same conditions of using Cu foil as the current collector, the trend in the electrochemical performance of the three alkali metals remains K > Li > Na. This observation is consistent with the phenomenon observed earlier when using Al as the current collector.

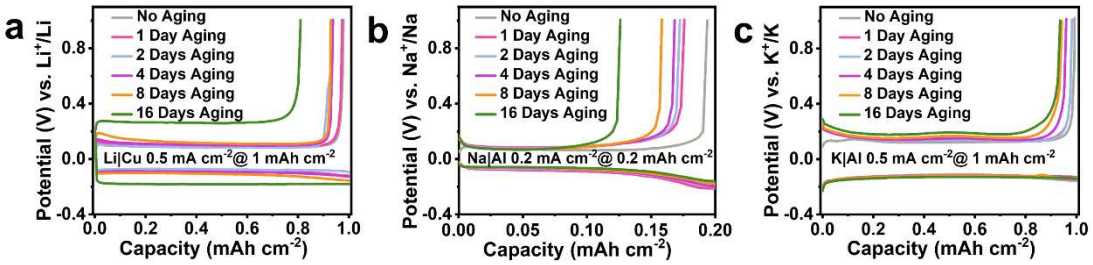

Fig. S9 Calendar aging behaviors of three alkali metals with controlled temperatures at 25 ± 0.5 °C. Stripping and plating curves after various aging durations of the (a) Li|Cu, (b) Na|Al, and (c) K|Al cells.

This aging test of the alkali metals was conducted as follows: first, the alkali metal was electroplated onto the current collector, then left at an open circuit condition for various durations, and finally stripped to the designated cutoff potential (1 V). By utilizing the plated capacity before aging and the stripped capacity after aging to calculate the CE, where CE = (stripped capacity after aging / plated capacity before aging) * 100%, the aging stability can be quantitatively assessed.

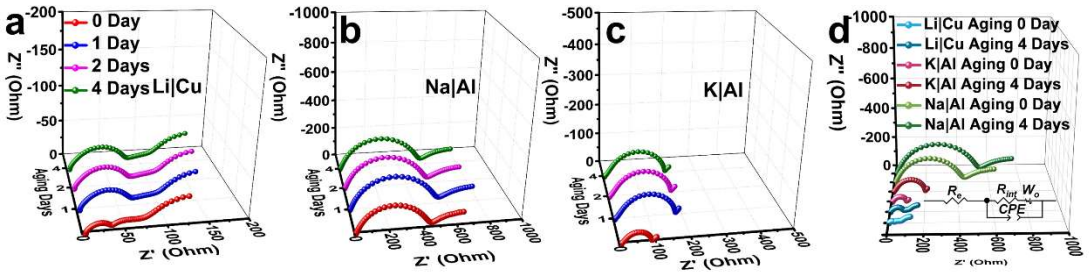

Fig. S10 (a-c) The Nyquist plots of the Li|Li, Na|Na and K|K symmetric cells after various aging durations. (d) A comparison of the Nyquist plots of the Li|Li, Na|Na and K|K symmetric cells after aging 4 days and no aging (insets: the equivalent circuit used to fit the Nyquist plots, where R_e, R_{int}, W_o, and *CPE* stand for electrolyte resistance, interfacial impedance, Warburg impedance, and constant phase element, respectively). The parameters obtained from EIS fitting are listed in Table S4.

In the Li|Cu and K|Al cells, the interfacial impedance R_{int}, represented by the diameter of the semicircle in the Nyquist plots, initially increased during aging and then exhibited minor variations with an extended aging duration, indicating the formation of a stable SEI in these two cells. Among the three cells, the Li|Cu cell displays the smallest impedance (Fig. S10a-c and Table S4), in agreement with its lowest polarization observed during the plating-stripping test. It is worth noting that the interfacial impedance of the Na|Al cell was the highest and showed little difference before and after calendar aging. Given the poor CE and aging stability of the Na|Al cell, this observation suggests that continuous side reactions occur between the Na metal and the electrolyte.

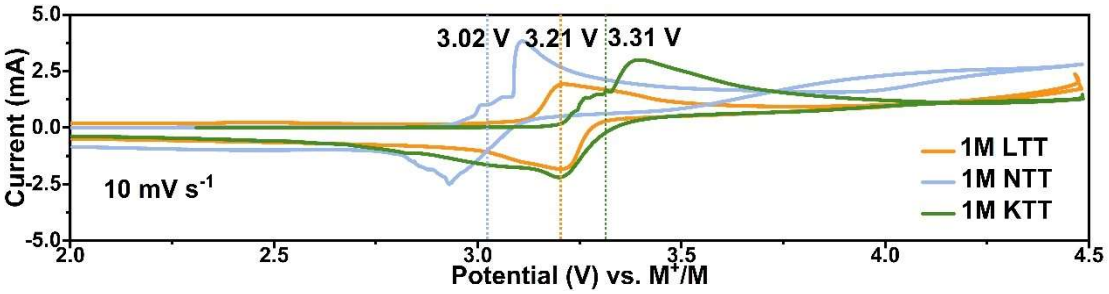

Fig. S11 The estimated electrode potential of M^+/M (M = Li, Na and K) for three alkali metal in their corresponding electrolytes.

The redox species ferrocene (Fc^+/Fc) served as an electrolyte-independent reference electrode.[17-19] As presented in Fig. S11, the estimated electrode potential of K^+/K, at -3.31 V *vs.* Fc^+/Fc, is the lowest among the three alkali metals, followed by Li^+/Li at -3.21 V *vs.* Fc^+/Fc, and the highest is associated with Na^+/Na at -3.02 V *vs.* Fc^+/Fc. In general, a lower electrode potential implies a greater thermodynamic driving force to reduce electrolytes, which, in turn, results in a lower deposition-stripping CE. However, it is important to note that, despite K exhibiting the lowest electrode potential, it displays the highest CE, underscoring the presence of a robust and stable SEI on the surface of K metal. Conversely, although Na has a relatively high electrode potential, it exhibits the lowest CE, indicating the formation of an unstable SEI on the Na metal surface.

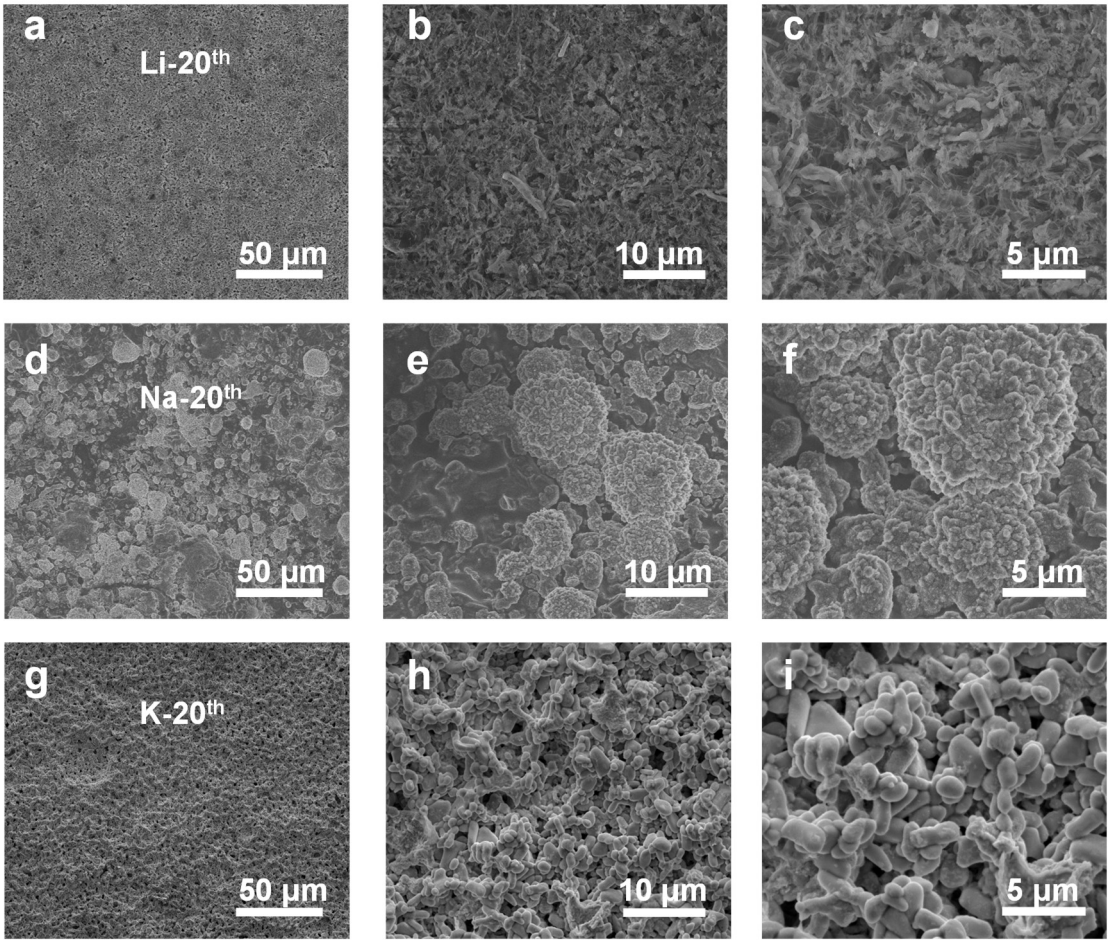

Fig. S12 Morphological characterization of the plated alkali metals. (a-c) SEM images of the plated Li metal on the Cu foil with the capacity of 0.5 mAh cm^{-2} after 20 cycles of pre-cycling. (d-f) SEM images of the plated Na metal on the Al foil with the capacity of 0.2 mAh cm^{-2} after 20 cycles of pre-cycling. (g-i) SEM images of the plated K metal on the Al foil with the capacity of 0.5 mAh cm^{-2} after 20 cycles of pre-cycling.

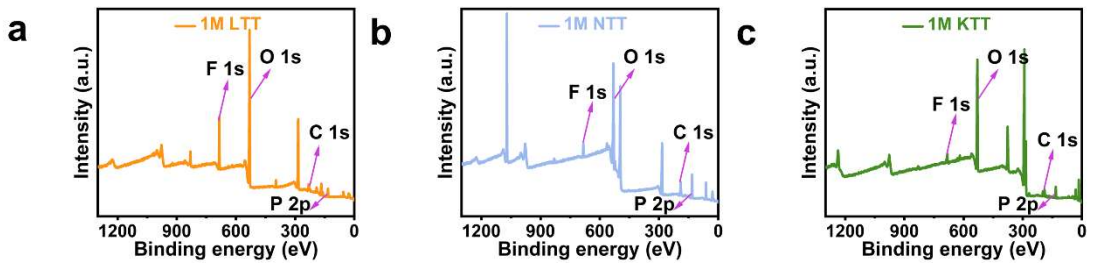

Fig. S13 The X-ray photoelectron spectroscopy (XPS) full spectrum of the surface of plated (a) Li, (b) Na, and (c) K.

The C 1s spectra (Fig. 3e) of three alkali metals can be deconvoluted into three peaks, representing C=O (288.8 eV), C-O (286.6 eV), and C-C (284.8 eV),[20] which are mainly originated from the degradation of electrolyte solvents. Notably, the relative intensity of the C-O peak to the C-C signal is considerably more pronounced in the Na SEI compared to that of the Li and K counterparts, indicating a higher abundance of organic components in the Na SEI. After argon ion etching, the content of each component experiences a substantial reduction. Even after a 50-second etching process, a faint C-O signal can still be detected for Li (as shown in Figure S14) and Na (as illustrated in Fig. S15), whereas it is conspicuously absent in the case of K (as seen in Fig. S16), suggesting a minimal presence of organic constituents in the K SEI. In the F 1s spectra presented in Fig. 3f, the peak signals can primarily be ascribed to S-F (at 687.4 eV) and M-F (M=Li (at 684.7 eV), Na (at 684.1 eV), K (at 682.9 eV)), both stemming from the decomposition of MFSI.[21, 22] As we progress from Li to Na to K, the contribution of S-F to the F 1s spectra exhibits an increasing trend, implying the involvement of more anions in the formation of the SEI. Following argon ion etching, the relative ratio of S-F to M-F (M=Li, Na, K) exhibits minor fluctuations for all three alkali metals, signifying that the SEI on these metals features a typical mosaic structure. In the O 1s spectra (Fig. 3g), the signals can be deconvoluted into four components characterized by binding energies of 532.8 eV, 531.7 eV, (531.8 eV, 530.7 eV, and 530.3 eV for Li, Na, and K, respectively), and 530.4 eV, corresponding to C-O, S-O, ($Li_xP_yO_z$, $Na_xP_yO_z$, $K_xP_yO_z$), and C=O functionalities. Additionally, a minor contribution of Li-O species is observed on the Li metal surface (as shown in Fig 3g).[21, 23-25] The mentioned phosphate

compounds primarily originate from the decomposition of TEP. Notably, the relative intensity ratio between the phosphates and the C-O peak is highest for K metal and lowest for Na metal, indicating a greater presence of organic compounds on the Na metal, in accordance with the C 1s spectra. After etching, the content of phosphates remains nearly unchanged, suggesting their uniform distribution within the SEI. The P 2p spectra further confirm the presence of phosphates (as depicted in Fig. 3h). In summary, the XPS spectra illustrate that the surface of Na metals contains more organic components, while that of Li and K metals consists primarily of inorganic components.

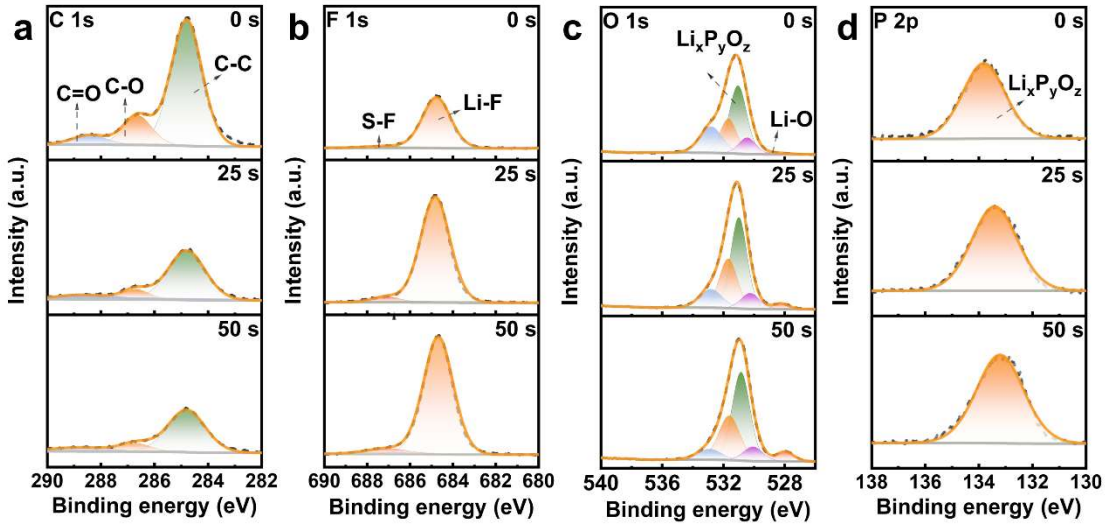

Fig. S14 The XPS analysis of deeply etched SEI formed on the Li metal with an areal plating capacity of 0.5 mAh cm^{-2}. The spectra of (a) C 1s, (b) F 1s, (c) O 1s, and (d) P 2p. Note: the number in the upper right corner of the subgraph represents the argon ion etching time.

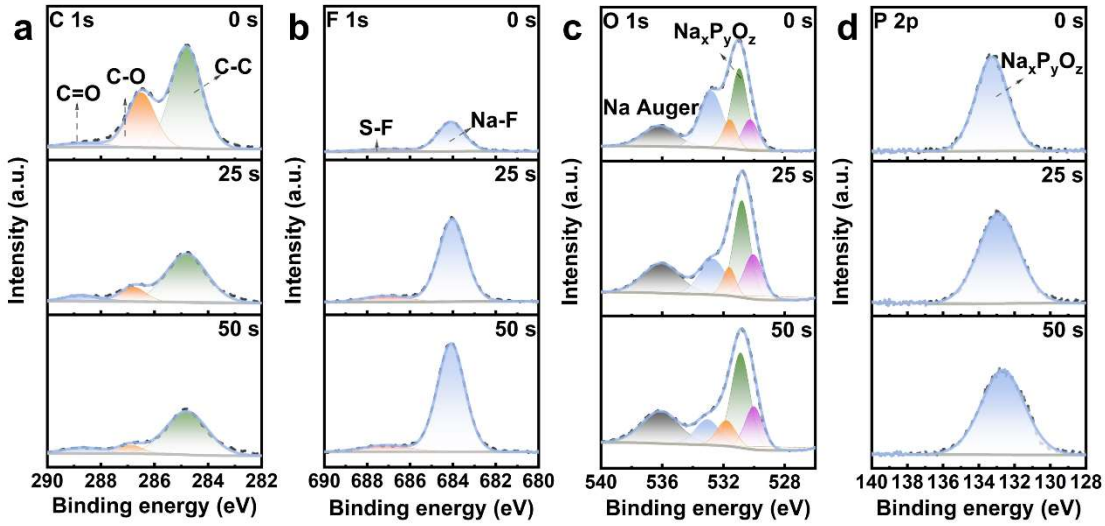

Fig. S15 The XPS analysis of deeply etched SEI formed on the Na metal with an areal plating capacity of 0.2 mAh cm^{-2}. The spectra of (a) C 1s, (b) F 1s, (c) O 1s, and (d) P 2p. Note: the number in the upper right corner of the subgraph represents the argon ion etching time.

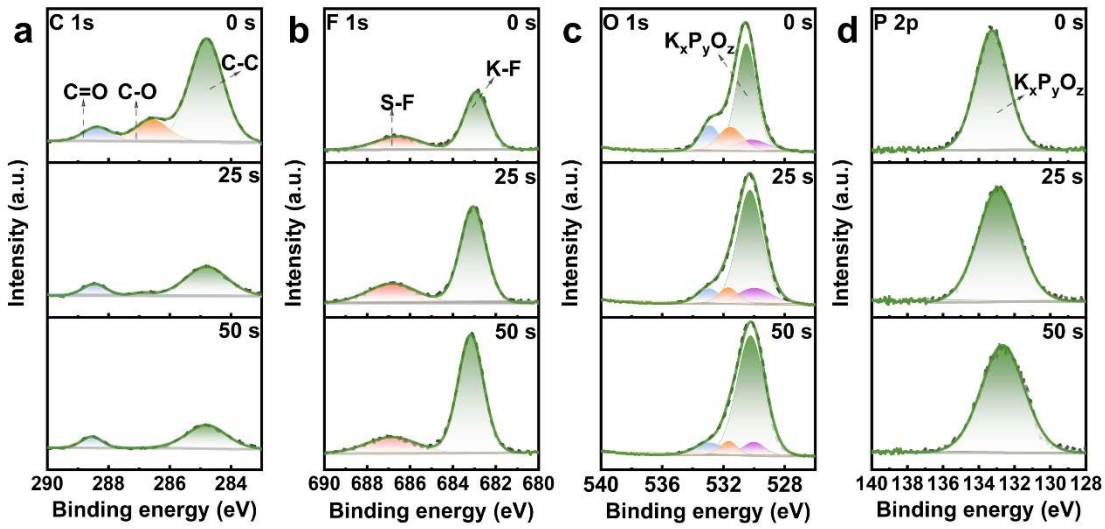

Fig. S16 The XPS analysis of deeply etched SEI formed the K metal with an areal plating capacity of 0.5 mAh cm^{-2}. The spectra of (a) C 1s, (b) F 1s, (c) O 1s, and (d) P 2p. Note: the number in the upper right corner of the subgraph represents the argon ion etching time.

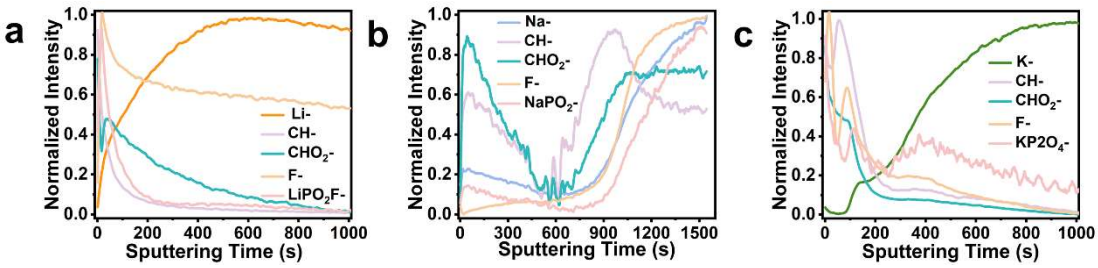

Fig. S17 Normalized (to maximum) depth profiles of various critical ion fragments observed on distinct alkali metal surfaces after 20 cycles. (a) Li, (b) Na, and (c) K.

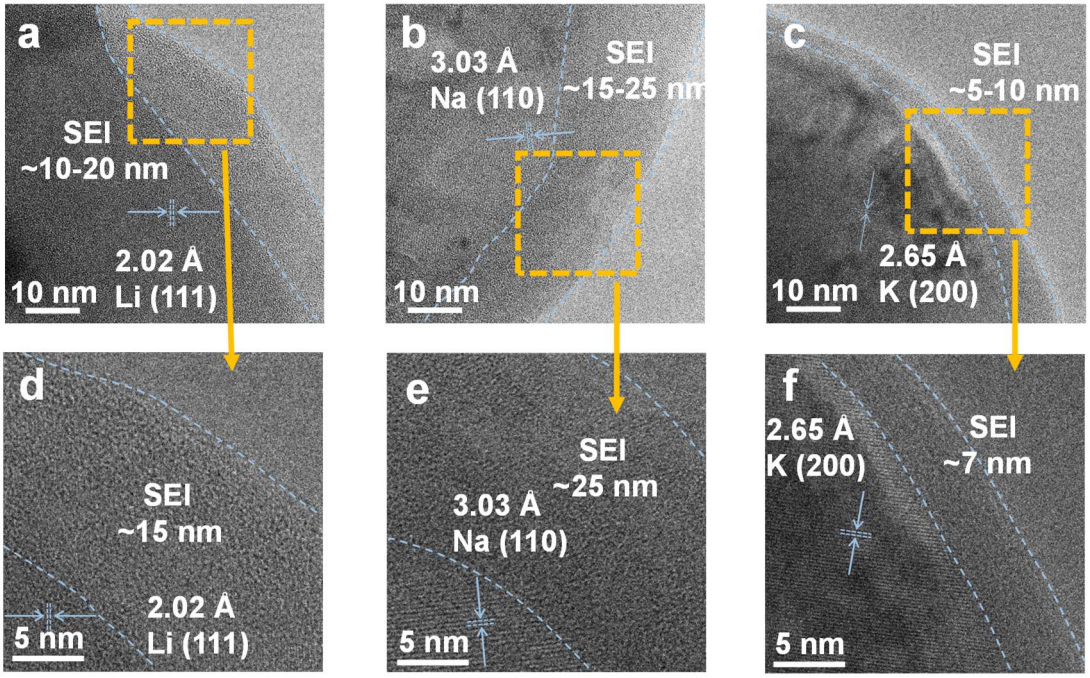

Fig. S18 Cryo-TEM images depicting the SEI nanostructure on the plated (a) Li, (b) Na, and (c) K metal. (d-f) Enlarged view marked by dashed squares in a-c to show SEI nanostructures observed on the surface of each respective alkali metal.

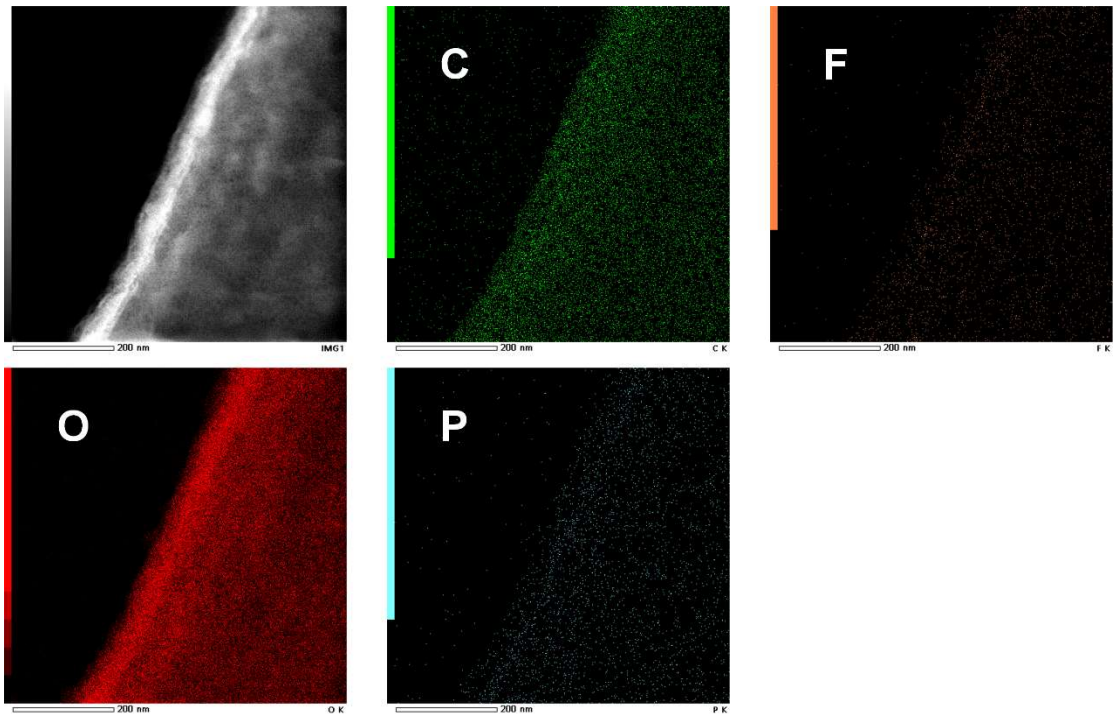

Fig. S19 Cryo-STEM image and the corresponding EDS elemental mapping of the deposited Li.

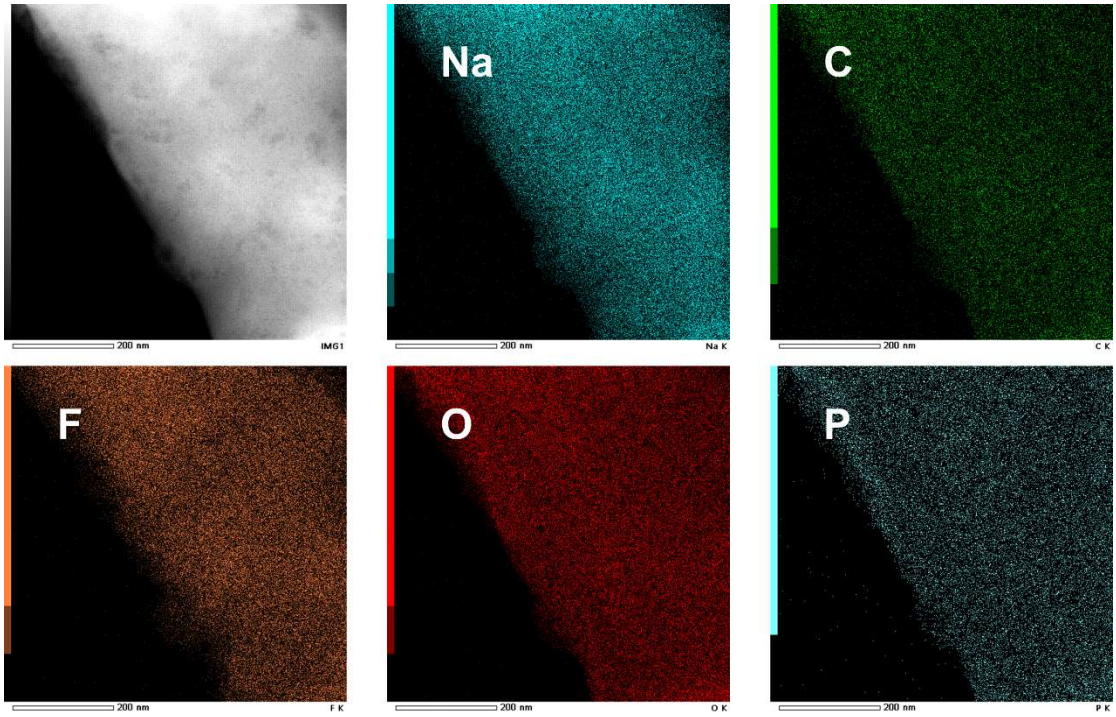

Fig. S20 Cryo-STEM image and the corresponding EDS elemental mapping of the deposited Na.

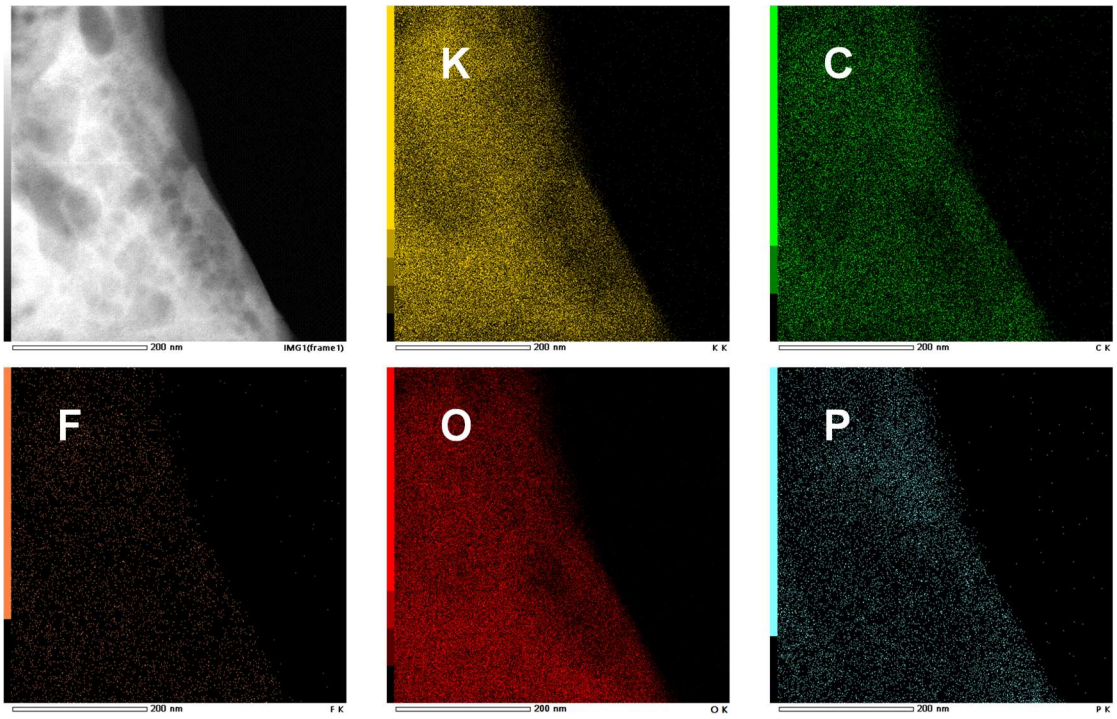

Fig. S21 Cryo-STEM image and the corresponding EDS elemental mapping of the deposited K.

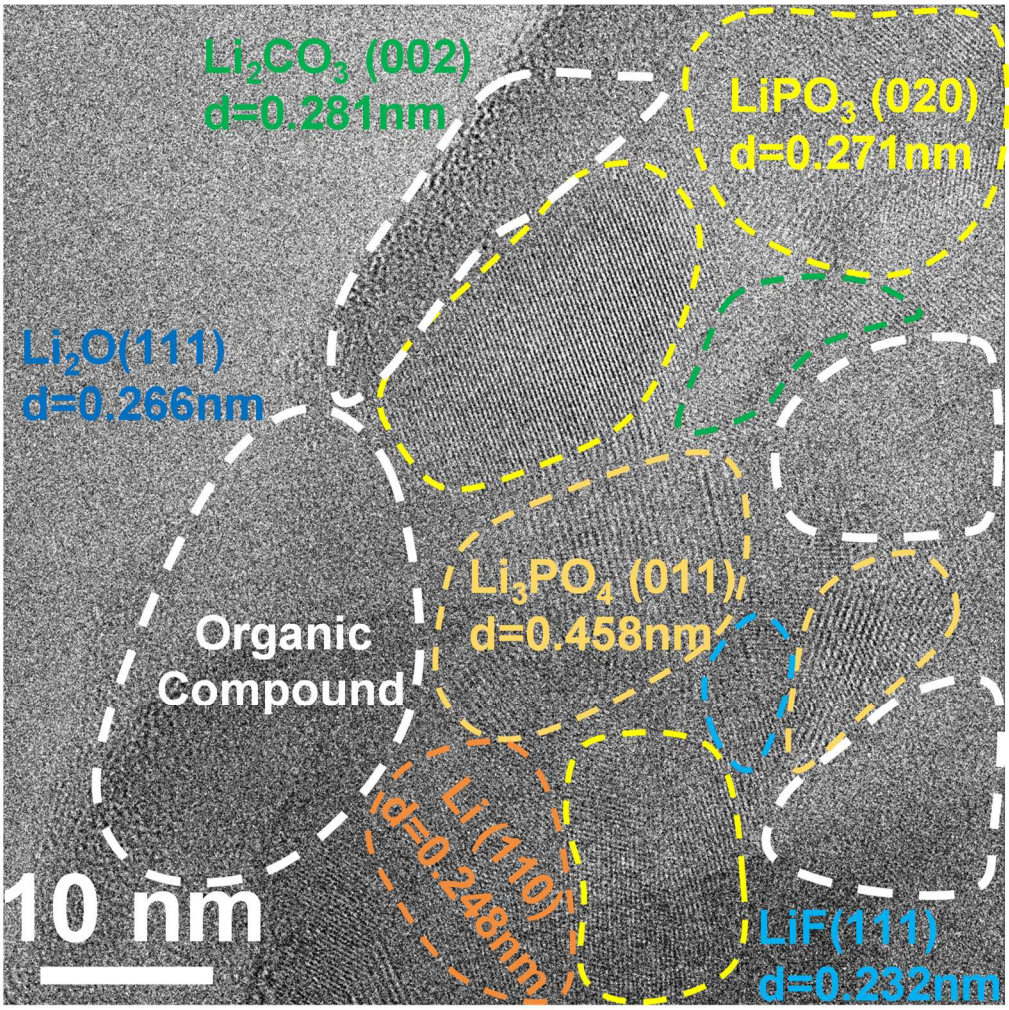

Fig. S22 The enlarged view of Fig. 4g.

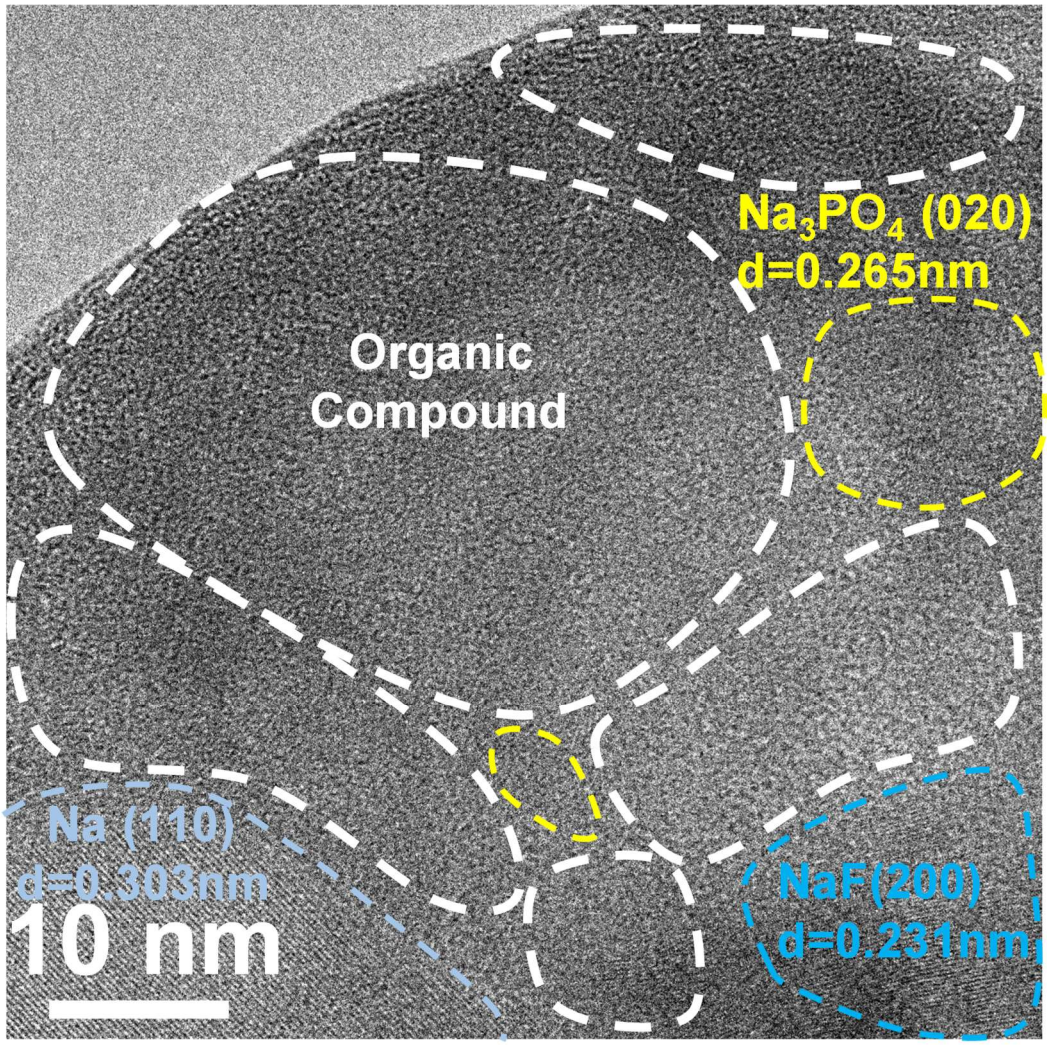

Fig. S23 The enlarged view of Fig. 4h.

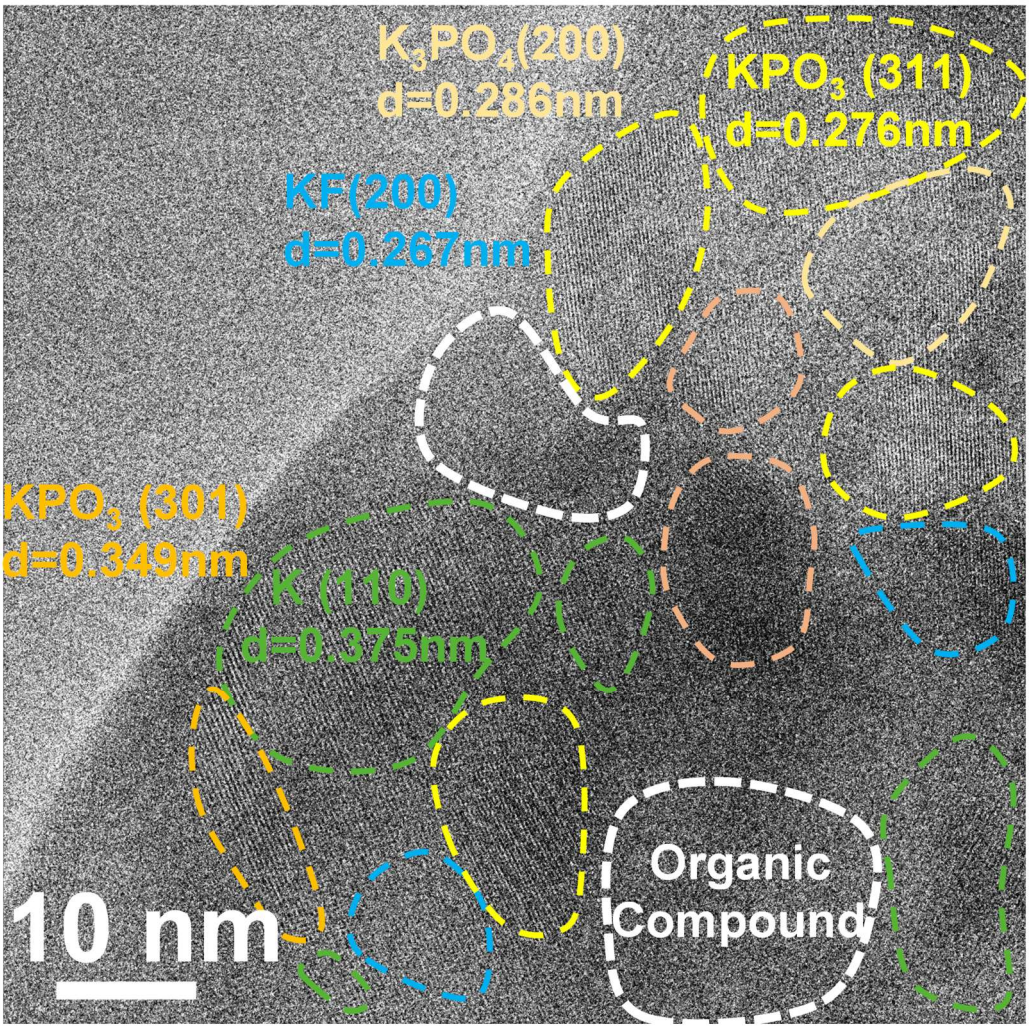

Fig. S24 The enlarged view of Fig. 4i.

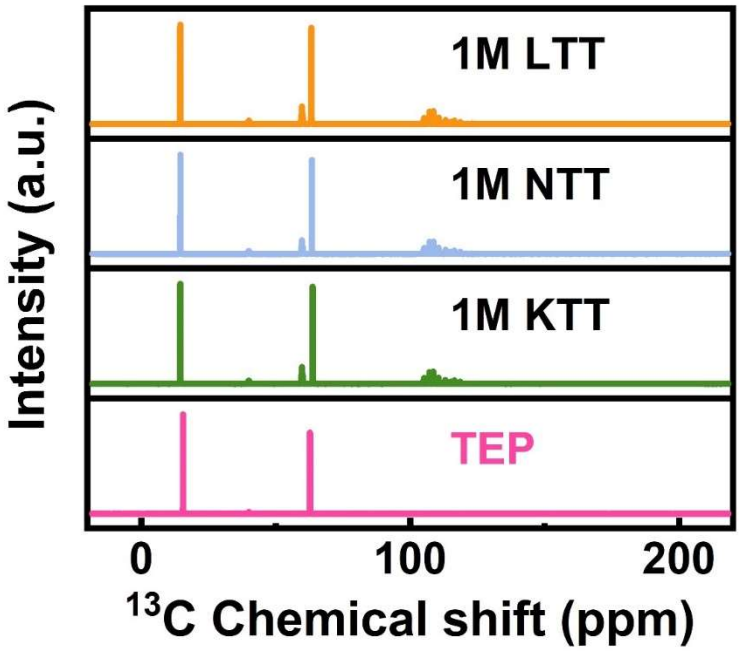

Fig. S25 The ^{13}C-NMR full spectrum of three electrolytes and pure TEP solvent.

Fig. 5b displays the ^{13}C-NMR results from the carbon atoms of the methyl CH_3 (right) and methylene CH_2 (left) groups in TEP. When TEP molecules coordinate with alkali metal ions, the electrons on the CH_2 group are rearranged, thus weakening the shielding effect of the ^{13}C extranuclear electrons on the ^{13}C nucleus.[20, 26] This de-shielding effect is subsequently manifested as the downfield shift of chemical shift in the NMR spectra. As shown in Fig. 5b (left), the chemical shift of ^{13}C nuclei around 62.7 ppm, representing the carbon of the CH_2 group in neat TEP, is shifted downfield to 63.7 ppm, 63.4 ppm, and 63.1 ppm for LTT, NTT, and KTT, respectively. This observation is consistent with the Raman spectroscopy results, indicating that the interaction between alkali metal ions and TEP follows the order of $Li^+ > Na^+ > K^+$. Besides, the peak corresponding to the carbon of the CH_3 group in neat TEP (15.5 ppm) shifted upfield significantly to 14.5 ppm (Fig. 5b right). This shift suggests the creation of an electron-rich environment around the CH_3 group, enhancing the electron shielding effect. This effect can be attributed to the incorporation of FSI^- anion into the solvation sheath, which increases the electron cloud density of the CH_3 group of TEP.[26]

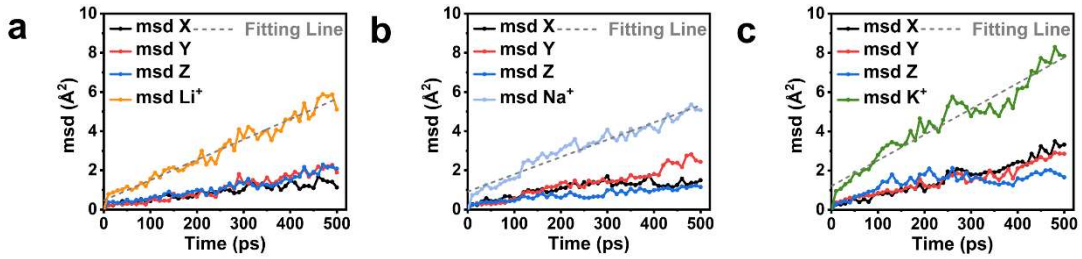

Fig. S26 The mean square displacement of cations derived from the cMD simulations (a) Li^+, (b) Na^+, (c) K^+.

Based on the mean square displacement of cations derived from the cMD simulations (as shown in Fig. S26), the cation diffusion coefficients are estimated to be $1.73x10^{-11}$, $1.47x10^{-11}$, and $2.18x10^{-11}$ m^2 s^{-1} for Li^+, Na^+, and K^+, respectively. The highest diffusion coefficient observed for K^+ can be attributed to its weaker interaction with TEP, which leads to the highest transference number among the three alkali metal ions (as seen in Fig. 1f). On the other hand, Na^+ exhibits the lowest diffusivity, explaining its smallest transference number in Fig. 1f. Even though Li^+ has a stronger interaction with TEP compared to Na^+, it displays a higher diffusion coefficient than Na^+. This could be attributed to the smaller ionic size of Li^+. Consequently, when FSI^- is incorporated into the primary solvation sheath of Li^+, the charge of Li^+ becomes more effectively screened, and the interaction of Li^+ with molecules beyond the primary solvation sheath is significantly weakened. This results in a smaller moving entity in the Li electrolyte compared to that in the Na electrolyte.

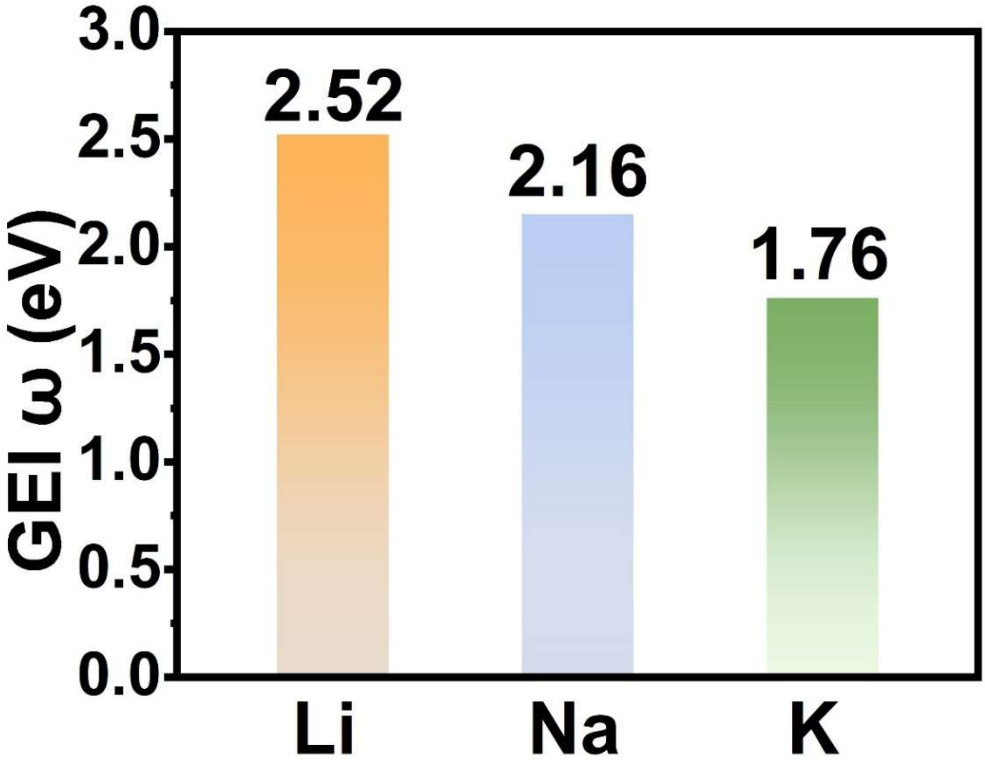

Fig. S27 The global electrophilicity indices of Li, Na, and K.

In the same electrolyte solvent (*i.e.*, Lewis base), the acidity of alkali ions (*i.e.*, Lewis acids) is actually the ability of Lewis acids to accept electrons from Lewis bases, which directly influences the interaction between alkali ions and electrolyte solvent, thereby affecting the solvation structure and ultimately the electrochemical performance of batteries.[27-31] In the literature, the Lewis acidity has been quantitatively analyzed using the global electrophilicity index (GEI) ω (Fig. S27),[32, 33] which is a measure of a Lewis acid's electron accepting ability and defined as:

$$\omega = \mu^2/2\eta = \chi^2/2\eta \quad (7)$$

where μ is the chemical potential, η is the chemical hardness,[34] and χ is electronegativity (the negative of chemical potential μ) of Lewis acids.[35] Therefore, the Lewis acidity is related to electronegativity and chemical hardness.[36] Electronegativity is related to both the ionic radius and electron cloud density, while chemical hardness is mainly determined by the ionization energy and electron affinity of molecules or ions.[35]

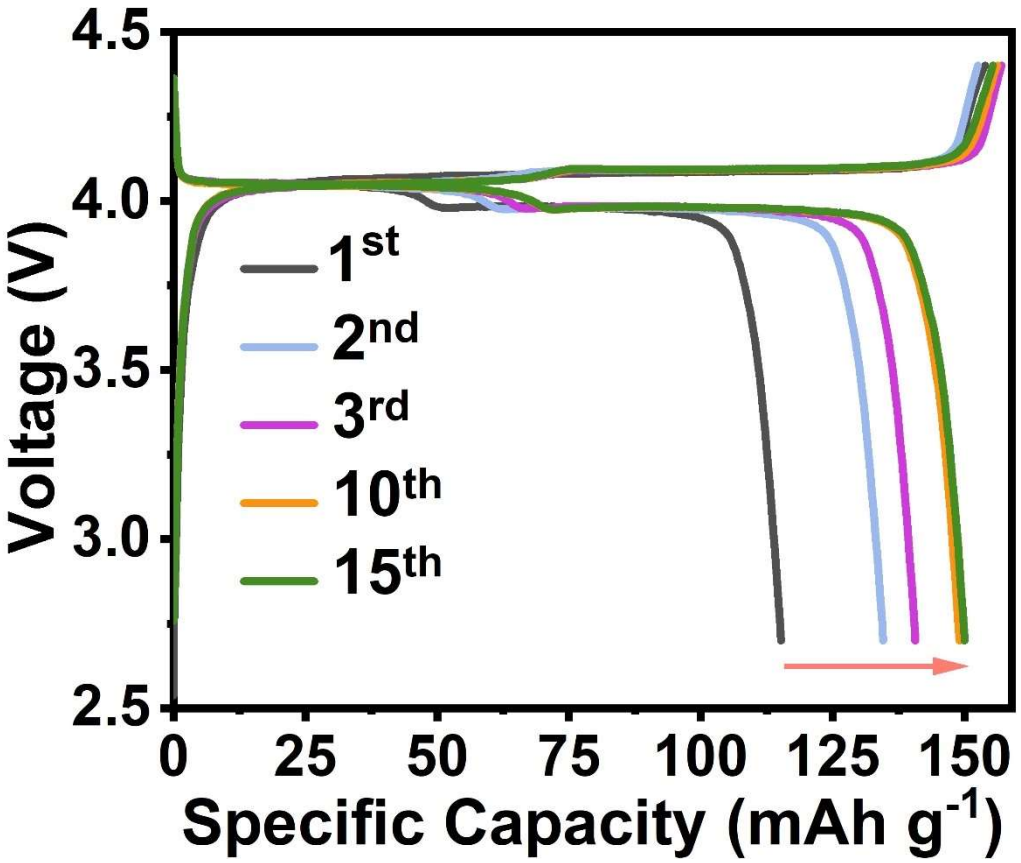

Fig. S28 Galvanostatic charge-discharge voltage curves of the K|KMF cell at 15 mA g^{-1}.

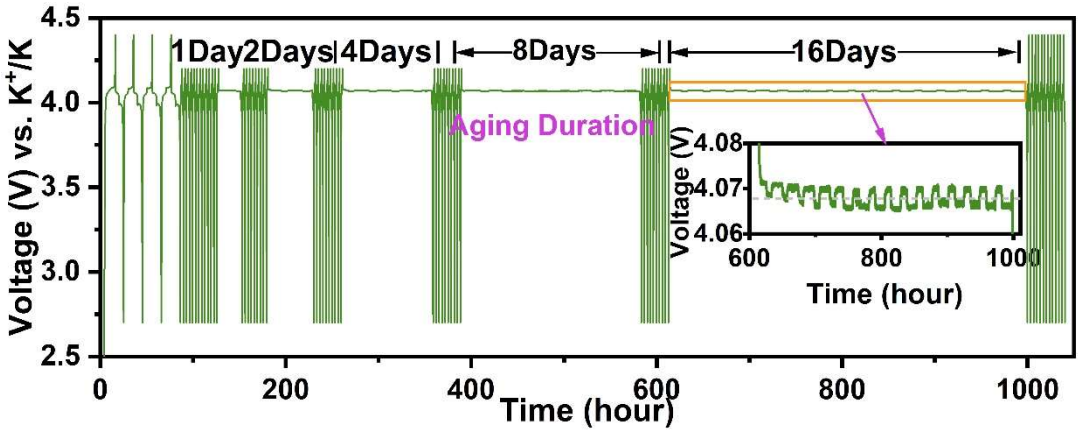

Fig. S29 The voltage-time curves of the K|KMF cell undergoing the self-discharge process for various durations, insets: the enlarged view of the voltage-time curves during the 16-days self-discharge process.

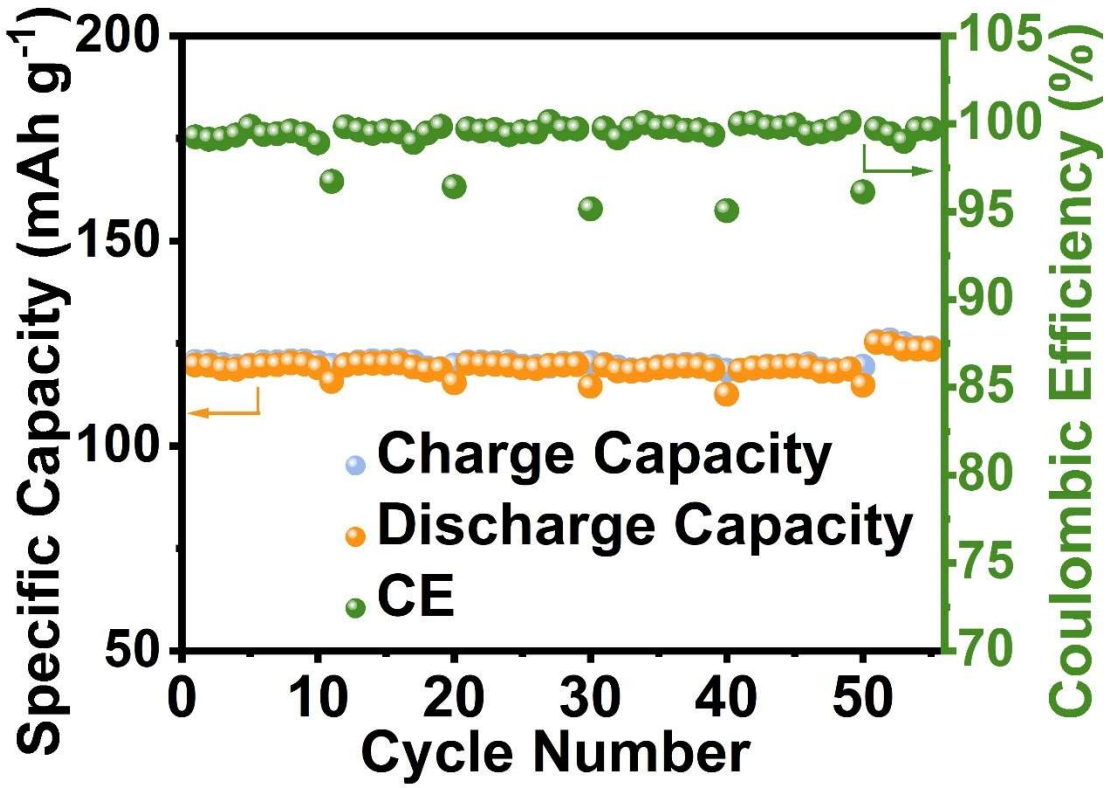

Fig. S30 Cycling performance of the K|KMF cell after various aging durations.

Table S1. Comparisons of electrochemical performance of different alkali metals tested in the electrolytes with similar compositions.

Cells	Electrolyte	Electrochemical Performance	Reference
Li|Cu	KFSI-1.4DME	Plating-stripping CE ~99.1%	[Ref1][37]
Na|Cu	5M NaFSI/DME	Plating- stripping CE ~99.1%	[Ref2][38]
Na|Cu	1M $NaPF_6$/DME	Plating- stripping CE ~99.9	[Ref3][38]
K|Cu	1M KFSI/DME	Plating- stripping CE ~99%	[Ref4][39]
Li|Cu	7M LiFSI/FEC	Plating- stripping CE ~99%	[Ref5][40]
Na|Cu	1M NaFSI/FEC	Plating- stripping CE ~94%	[Ref6][41]
K|Cu	0.8M KPF_6/EC+DEC+5 wt% FEC	Plating- stripping CE ~70%	[Ref7][42]
K|HC	0.8M KFSI/EC+PC+5 wt% FEC	extremely poor with a specific capacity 3mAh g^{-1}	[Ref8][43]
Li|Cu	**1M LiFSI/TEP+TTE**	**Plating- stripping CE ~87.36%**	**This work**
Na|Al	**1M NaFSI/TEP+TTE**	**Plating- stripping CE ~31.36%**	**This work**
K|Al	**1M KFSI/TEP+TTE**	**Plating- stripping CE ~99.33%**	**This work**

Table S2. The cell parameters used in Eqs. (3) and (4).

Electrolyte	d (mm)	$m_{\ln}$	F	R	T (K)	A (cm^2)	ε	c_0 (mol L^{-1})	$U(t_1)$ (V)	t_1	I_P (mA)	b	U_{CC} (V)	Δc	a	t_+
		0.00222							0.0335			2.51				0.694
LTT		0.00246				2.01			0.03995			3.16	0.0849		8.21	0.616
		0.00164							0.0405			2.61				0.682
		0.000883							0.0753			2.73				0.286
NTT	0. 675	0.000749	96485.3	8.314	299	1.539	40%	1	0.0674	900	0.3	2.25	0.0395	0.1	3.82	0.412
		0.00136							0.0375			1.69				0.559
		0.000941							0.0546			1.33				0.696
KTT		0.00107				1			0.05678			1.47	0.045		4.37	0.663
		0.000947							0.05577			1.36				0.689

Table S3. Coulombic efficiency of three alkali metals tested in the corresponding electrolytes.

Cell type	Areal capacity (mAh cm^{-2})	Average CE (%)	1st CE (%)	20th-100th average CE (%)	Average cycling CE (%)
Li|Cu	0.2	88.5	84.41	97.97	8th-130th 97.8
Na|Al	0.2	93.34	5.19	96.38	33th-130th 96.73
K|Al	0.2	98.96	66.19	99.15	20th -510th 99.07
Li|Cu	1	87.76	93.23	--	2nd-19th 97.44
Na|Al	1	31.36	44.23	--	--
K|Al	1	99.33	86.14	99.49	10th-250th 99.47

Table S4. The impedance data obtained from alkali metal cells after aging.

Li|Cu			Na|Al			K|Al		
Aging Duration	R_e	R_{int}	Aging Duration	R_e	R_{int}	Aging Duration	R_e	R_{int}
0	4.981	31.23	0	10.86	436.8	0	8.314	85.34
1	4.888	68.1	1	10.83	541.6	1	8.263	185.4
2	4.968	76.12	2	10.78	532.3	2	8.260	198.7
4	5.011	82.4	4	10.83	543.9	4	8.131	204.6

Table S5. Specific energy of some recently reported K metal cells.

K metal cells	Electrolyte	Average discharge voltage (V)	anode-to-cathode capacity ratio*	Discharge capacity** (mAh g^{-1})	Stack-level specific energy*** (Wh kg^{-1})
rGO-K|$K_{0.22}Fe[Fe(CN)_6]_{0.805}$[44]	0.8M KPF_6 EC/DEC	3.4	2:1	55.3	94
K@Bi_{60}/NrGO|PB[45]	3M KFSI DME	3.1	2:1	68.4	106
K@EMS|PB[46]	3M KFSI DME	3	2:1	83.2	125
K|KPB[47]	1M KFSI DEGDME	3.3	2:1	51.8	85.5
K Cu@SKS|PBA[48]	4M KFSI DME	3.4	2:1	53.9	91.5
K|PBA[49]	1M KFSI G4/TTE	2.8	2:1	60.9	85
CoZn@HCT@K|PTCDA[50]	1M KFSI DME	2.6	2:1	96.3	98
K|KMCEC@rGO[51]	KCl-buffered $AlCl_3$/[3MIm]Cl	3.8	2:1	76.8	125
K|PB[52]	2.3M KFSI+50mM KNO3 DME	3.4	2:1	83.2	147.5
K|KPB[53]	0.8M KPF_6 EC/DEC	3.4	2:1	88.6	141.5

	+0.01% ATPPB				
K|PTCDA[54]	0.1M $KBPh_4$ EC/DEC	2.4	2:1	81.8	98
K@NGM|PB/G[55]	KFSI:DME=0.5	3.6	2:1	79.6	143
K/Pd/Cu|PB[56]	3M KFSI DME	3	2:1	51.34	77
K|KMF[57]	1M KFSI DIDBE+6%DTD	3.8	4:1	70.55	134
This work	**1M KFSI TEP/TTE**	**3.94**	**2:1**	**104.3**	**206**

* As most literature does not specify the actual N/P ratio, we assume an N/P ratio of 2:1. However, in practical experiments, an excess of potassium metal is typically present, resulting in the actual N/P ratio being significantly higher than 2:1.

** The discharge capacity is calculated based on the total mass of cathode and anode materials in the cells.

*** The stack-level specific energy of the batteries is estimated by halving the specific energy values which are calculated based on the total mass of cathode and anode materials in the corresponding batteries.[58]

References

1. L. Deng, J. Qu, X. Niu, J. Liu, J. Zhang, Y. Hong, M. Feng, J. Wang, M. Hu, L. Zeng, Q. Zhang, L. Guo and Y. Zhu, *Nature Communications*, 2021, **12**, 2167 (2021).
2. Y. Chen, Y. Zhu, Y. Ruan, N. Zhao, W. Liu, W. Zhuang and X. Lu, *Carbon*, 2019, **144**, 32-42.
3. S. V. Sambasivarao and O. Acevedo, *J. Chem. Theory Comput.*, 2009, **5**, 1038-1050.
4. L. S. Dodda, I. Cabeza de Vaca, J. Tirado-Rives and W. L. Jorgensen, *Nucleic Acids Research*, 2017, **45**, W331-W336.
5. L. Martínez, R. Andrade, E. G. Birgin and J. M. Martínez, *Journal of Computational Chemistry*, 2009, **30**, 2157-2164.
6. A. I. Jewett, D. Stelter, J. Lambert, S. M. Saladi, O. M. Roscioni, M. Ricci, L. Autin, M. Maritan, S. M. Bashusqeh, T. Keyes, R. T. Dame, J.-E. Shea, G. J. Jensen and D. S. Goodsell, *Journal of Molecular Biology*, 2021, **433**, 166841.
7. M. Frisch, G. Trucks, H. Schlegel, G. Scuseria, M. Robb, J. Cheeseman, G. Scalmani, V. Barone, G. Petersson and H. Nakatsuji, *Journal*, 2016.
8. T. Lu and F. Chen, *Journal of Computational Chemistry*, 2011, **33**, 580-592.
9. S. Amara, J. Toulc'Hoat, L. Timperman, A. Biller, H. Galiano, C. Marcel, M. Ledigabel and M. Anouti, *ChemPhysChem*, 2019, **20**, 581-594.
10. C. Austen Angell, Y. Ansari and Z. Zhao, *Faraday Discuss.*, 2012, **154**, 9-27.
11. M. P. Longinotti and H. R. Corti, *J. Phys. Chem. B*, 2009, **113**, 5500-5507.
12. Y. Matsuda, H. Nakashima, M. Morita and Y. Takasu, *Journal of The Electrochemical Society*, 1981, **128**, 2552.
13. J. Landesfeind and H. A. Gasteiger, *Journal of The Electrochemical Society*, 2019, **166**, A3079-A3097.
14. A. Ehrl, J. Landesfeind, W. A. Wall and H. A. Gasteiger, *Journal of The Electrochemical Society*, 2017, **164**, A2716-A2731.
15. A. Ehrl, J. Landesfeind, W. A. Wall and H. A. Gasteiger, *Journal of The Electrochemical Society*, 2017, **164**, A826-A836.
16. P. Liu, Y. Wang, H. Hao, S. Basu, X. Feng, Y. Xu, J. A. Boscoboinik, J. Nanda, J. Watt and D. Mitlin, *Advanced Materials*, 2020, **32**, A826-A836.
17. S. Ko, T. Obukata, T. Shimada, N. Takenaka, M. Nakayama, A. Yamada and Y. Yamada, *Nature Energy*, 2022, **7**, 1217-1224.
18. J. Landesfeind, A. Ehrl, M. Graf, W. A. Wall and H. A. Gasteiger, *Journal of The Electrochemical Society*, 2016, **163**, A1254-A1264.
19. N. Mozhzhukhina and E. J. Calvo, *Journal of The Electrochemical Society*, 2017, **164**, A2295-A2297.
20. Y. X. Yao, X. Chen, C. Yan, X. Q. Zhang, W. L. Cai, J. Q. Huang and Q. Zhang, *Angewandte Chemie International Edition*, 2020, **60**, 4090-4097.
21. J. Zhang, H. Zhang, L. Deng, Y. Yang, L. Tan, X. Niu, Y. Chen, L. Zeng, X. Fan and Y. Zhu, *Energy Storage Materials*, 2023, **54**, 450-460.
22. Y. Lee, T. K. Lee, S. Kim, J. Lee, Y. Ahn, K. Kim, H. Ma, G. Park, S.-M. Lee, S. K. Kwak and N.-S. Choi, *Nano Energy*, 2020, **67**, 104309.
23. X. Zhou, Q. Zhang, Z. Zhu, Y. Cai, H. Li and F. Li, *Angew Chem Int Ed Engl*, 2022, **61**,

e202205045.
24. W. E. Morgan, J. R. Van Wazer and W. J. J. J. o. t. A. C. S. Stec, 1973, **95**, 751-755.
25. X. Huang, R. Li, C. Sun, H. Zhang, S. Zhang, L. Lv, Y. Huang, L. Fan, L. Chen, M. Noked and X. Fan, *ACS Energy Letters*, 2022, **7**, 3947-3957.
26. W. W. A. van Ekeren, M. Albuquerque, G. Ek, R. Mogensen, W. R. Brant, L. T. Costa, D. Brandell and R. Younesi, *Journal of Materials Chemistry A*, 2023, **11**, 4111-4125.
27. M. Okoshi, Y. Yamada, A. Yamada and H. Nakai, *Journal of The Electrochemical Society*, 2013, **160**, A2160-A2165.
28. T. A. Pham, K. E. Kweon, A. Samanta, V. Lordi and J. E. Pask, *The Journal of Physical Chemistry C*, 2017, **121**, 21913- 21920.
29. K. Miyazaki, N. Takenaka, E. Watanabe, Y. Yamada, Y. Tateyama and A. Yamada, *ACS Appl Mater Interfaces*, 2020, **12**, 42734-42738.
30. M. Okoshi, Y. Yamada, S. Komaba, A. Yamada and H. Nakai, *Journal of The Electrochemical Society*, 2016, **164**, A54-A60.
31. F. Sagane, T. Abe, Y. Iriyama and Z. Ogumi, *Journal of Power Sources*, 2005, **146**, 749-752.
32. A. T. Maynard, M. Huang, W. G. Rice and D. G. Covell, 1998, **95**, 11578-11583.
33. A. R. Jupp, T. C. Johnstone and D. W. Stephan, *Dalton Transactions*, 2018, **47**, 7029-7035.
34. R. G. Parr and R. G. Pearson, *Journal of the American Chemical Society*, 1983, **105**, 7512-7516.
35. R. S. Mulliken, *The Journal of Chemical Physics*, 1934, **2**, 782-793.
36. R. G. Pearson, *Journal of Chemical Sciences*, 2005, **117**, 369-377.
37. X. Ren, L. Zou, S. Jiao, D. Mei, M. H. Engelhard, Q. Li, H. Lee, C. Niu, B. D. Adams, C. Wang, J. Liu, J.-G. Zhang and W. Xu, *ACS Energy Letters*, 2019, **4**, 896-902.
38. Z. W. Seh, J. Sun, Y. Sun and Y. Cui, *ACS Central Science*, 2015, **1**, 449-455.
39. N. Xiao, W. D. McCulloch and Y. Wu, *Journal of the American Chemical Society*, 2017, **139**, 9475-9478.
40. L. Suo, W. Xue, M. Gobet, S. G. Greenbaum, C. Wang, Y. Chen, W. Yang, Y. Li and J. Li, *Proceedings of the National Academy of Sciences*, 2018, **115**, 1156-1161.
41. Y. Lee, J. Lee, J. Lee, K. Kim, A. Cha, S. Kang, T. Wi, S. J. Kang, H.-W. Lee and N.-S. Choi, *ACS Applied Materials & Interfaces*, 2018, **10**, 15270-15280.
42. S. Baek, S. Jie and B. Lee, *Journal of Mechanical Science and Technology*, 2023, DOI: 10.1007/s12206-023-0630-3.
43. A. W. Ells, R. May and L. E. Marbella, *ACS Applied Materials & Interfaces*, 2021, **13**, 53841-53849.
44. Z. Wei, A. Wang, X. Guan, G. Li, Z. Yang, C. Huang, J. Zhang, L. Ren, J. Luo and X. Liu, *Energy & Environmental Materials*, 2022, **5**, 1278-1284.
45. Y. Feng, A. M. Rao, J. Zhou and B. Lu, *Advanced Materials*, 2023, **35**, 2300886.
46. H. Ding, J. Wang, J. Zhou, C. Wang and B. Lu, *Nature Communications*, 2023, **14**, 2305.
47. W. Xu, H. Wang, J. Hu, H. Zhang, B. Zhang, F. Kang and D. Zhai, *Chemical Communications*, 2021, **57**, 1034-1037.
48. J. Xie, Y. Ji, L. Ma, Z. Wen, J. Pu, L. Wang, S. Ding, Z. Shen, Y. Liu, J. Li, W. Mai and G. Hong, *ACS Nano*, 2023, **17**, 1511-1521.
49. C. Chen, J. Zhou, W. Gong, X. Fan, X. Meng, S. Chen, L. Sun, Y. Meng, K. Tao, B. Ülgüt, P. Sun, C. W. Bielawski and J. Geng, *ACS Applied Energy Materials*, 2022, **5**, 10366-10374.
50. G. Cheng, S. Liu, X. Wang, X. Li, Y. Su, J. Shi, M. Huang, Z. Shi, H. Wang and Z. Yan, *ACS*

Applied Materials & Interfaces, 2022, **14**, 45364-45372.

51. H. Sun, P. Liang, G. Zhu, W. H. Hung, Y.-Y. Li, H.-C. Tai, C.-L. Huang, J. Li, Y. Meng, M. Angell, C.-A. Wang and H. Dai, *Proceedings of the National Academy of Sciences*, 2020, **117**, 27847-27853.
52. H. Wang, J. Dong, Q. Guo, W. Xu, H. Zhang, K. C. Lau, Y. Wei, J. Hu, D. Zhai and F. Kang, *Energy Storage Materials*, 2021, **42**, 526-532.
53. Y. Jiang, S. Lu, J. Jiang, M. Li, Y. Liao, Y. Xu, S. Huang, B. Zhao and J. Zhang, *Small*, 2023, **19**, 2300411.
54. Q. Liu, M. Geng, T. Yu, L. Zhang, C. Wu, J. Liu, S. Zhao, Q. Yang, R. Song, J. Ye, F. Wang, Y. Wu, D. Xiao and Y. Chen, *Nano Research*, 2022, **16**, 8290-8296.
55. J. Xiong, M. Ye, Z. Wang, J. Chen, Y. Zhang, Y. Tang and C. C. Li, *Chemical Engineering Journal*, 2022, **442**, 2300411.
56. J. Wang, W. Yan and J. Zhang, *Nano Energy*, 2022, **96**, 107131.
57. Z. Yu, K. Fan, Q. Liu, D. Wang, C. Chen, Y. Zhu, H. Huang and B. Zhang, *Advanced Functional Materials*, 2024, DOI: 10.1002/adfm.202315446.
58. L. Jiang, Y. Lu, C. Zhao, L. Liu, J. Zhang, Q. Zhang, X. Shen, J. Zhao, X. Yu, H. Li, X. Huang, L. Chen and Y.-S. Hu, *Nature Energy*, 2019, **4**, 495-503.